

Journal of Biomedical Optics

BiomedicalOptics.SPIEDigitalLibrary.org

Reduced temporal sampling effect on accuracy of time-domain fluorescence lifetime Förster resonance energy transfer

Travis Omer
Lingling Zhao
Xavier Intes
Juergen Hahn

Reduced temporal sampling effect on accuracy of time-domain fluorescence lifetime Förster resonance energy transfer

Travis Omer,^a Lingling Zhao,^a Xavier Intes,^a and Juergen Hahn^{b,*}

^aRensselaer Polytechnic Institute, Department of Biomedical Engineering, 110 8th Street, Troy, New York 12180, United States

^bRensselaer Polytechnic Institute, Departments of Biomedical Engineering and Chemical & Biological Engineering, 110 8th Street, Troy, New York 12180, United States

Abstract. Fluorescence lifetime imaging (FLIM) aims at quantifying the exponential decay rate of fluorophores to yield lifetime maps over the imaged sample. When combined with Förster resonance energy transfer (FRET), the technique can be used to indirectly sense interactions at the nanoscale such as protein–protein interactions, protein–DNA interactions, and protein conformational changes. In the case of FLIM-FRET, the fluorescence intensity decays are fitted to a biexponential model in order to estimate the lifetime and fractional amplitude coefficients of each component of the population of the donor fluorophore (quenched and nonquenched). Numerous time data points, also called temporal or time gates, are typically employed for accurately estimating the model parameters, leading to lengthy acquisition times and significant computational demands. This work investigates the effect of the number and location of time gates on model parameter estimation accuracy. A detailed model of a FLIM-FRET imaging system is used for the investigation, and the simulation outcomes are validated with *in vitro* and *in vivo* experimental data. In all cases investigated, it is found that 10 equally spaced time gates allow robust estimation of model-based parameters with accuracy similar to that of full temporal datasets (90 gates). © 2014 Society of Photo-Optical Instrumentation Engineers (SPIE) [DOI: 10.1117/1.JBO.19.8.086023]

Keywords: fluorescence lifetime imaging; Förster resonance energy transfer; time-resolved imaging.

Paper 140371R received Jun. 10, 2014; revised manuscript received Jul. 16, 2014; accepted for publication Jul. 30, 2014; published online Aug. 28, 2014.

1 Introduction

Optical molecular imaging techniques based on fluorescence signals provide an invaluable tool to probe the cell and tissue biochemistries. Fluorescence lifetime imaging (FLIM), in particular, is increasingly useful over a broad range of applications spanning from fundamental biology to clinical diagnosis. Lifetime is an intrinsic property of a fluorophore and, therefore, does not typically depend on the method of measurement employed, fluorophore concentration, or fluorescence intensity.^{1–3} Lifetime, however, is dependent on the fluorophore structure and external factors such as temperature, viscosity, and polarity.² This makes fluorescence lifetime a complementary method to traditional fluorescence intensity measurements that can provide additional information to distinguish fluorophore species and/or to noninvasively monitor a microenvironment.^{4,5} Moreover, when coupled with Förster resonance energy transfer (FRET), FLIM enables the sensing and quantifying of protein–protein interactions, cell signaling processes, and other nanometer-range events.^{6–12} FRET relies on the nonradiative transfer of energy from an excited “donor” fluorophore to that of an “acceptor” when the two are within close proximity (2 to 10 nm).¹³ The energy transfer results in a measureable reduction in the fluorescence lifetime of the donor fluorophore.¹⁴ It is possible to obtain a quantitative estimate of the FRET efficiency in a sample by measuring the fluorescence lifetime of the donor fluorophore, which provides insight into the cellular processes being investigated. However, FRET

based on FLIM is still mainly confined to microscopy applications with visible fluorophore FRET pairs and long acquisition times. In order to translate FRET assays to high-throughput *in vitro* and *in vivo* applications for drug discovery,^{15,16} it is critical to identify strategies that will decrease measurement acquisition times without compromising quantitative FLIM-FRET analysis.

FLIM relies on the quantitative estimation of the fluorescence lifetime of a fluorophore from collected fluorescence intensity decays. Various methods exist for measuring the fluorescence lifetime of a fluorophore, though they generally fall into one of two major categories: frequency domain or time domain. Each works on the same basic principle of exposing the fluorophore to light within its excitation spectrum and then recording the resulting light the fluorophore emits. Frequency-domain FLIM uses a temporally modulated (often sinusoidal) excitation light and works at high intensities where time-domain methods are difficult to implement.¹⁷ Conversely, for applications with low concentrations and/or dim fluorescence signals, time-domain approaches should be favored, as they provide better signal-to-noise ratios.¹⁸

In time-domain FLIM, fluorophores are excited by short-light pulses, and the resulting fluorescence photons emitted are measured over time at different time delays (usually on the picosecond or nanosecond time scale). The resulting measurements correspond to the number of photons emitted, grouped into time bins. Photon counting or time-gated intensifier systems are primarily used to acquire these time-resolved

*Address all correspondence to: Juergen Hahn, E-mail: hahnj@rpi.edu

intensity measurements. Fluorescent lifetime can then be estimated through a variety of fitting or estimation methods applied to the experimental decay curves. Depending on the population of the sample or the number of states of the fluorophores in the sample, monoexponential or biexponential models are employed as models. In all cases, the measured fluorescence signals via time-domain systems are a combination of the pure fluorescence decay of the sample and the instrument response function (IRF) of the imaging system. The most common approach, which takes into account the temporal effect of the imaging system characteristics, consists of fitting the measurement to an exponential-decay model convolved with an experimental IRF using a least-squares (LSQR) method.¹⁹ An alternate method to exponential fitting is rapid lifetime determination (RLD). Originally developed for single-exponential decays,²⁰ RLD has been expanded and applied to double-exponential decays²¹ for applications such as FRET. RLD uses integrated areas underneath the decay curve to calculate model parameters. As this approach relies on simple algebraic equations, it is considerably faster than iterative fitting methods. A major drawback, however, is that RLD assumes the IRF of the system to be negligible.¹⁹ This assumption can hold for some visible FRET pairs that exhibit lifetimes of a few nanoseconds compared with the typical ~250- to 300-ps widths of experimental IRFs. However, this is not the case when using FRET pairs that are red shifted. These FRET pairs are critical for *in vivo* applications, as the near-infrared (NIR) spectral window corresponds to the lowest attenuation of photons in biotissues.^{22,23} For NIR FRET pairs, the lifetime reduces to a nanosecond or below, with the short-lifetime component associated with the FRETing donor being in the 250- to 350-ps²⁴ range. For such applications, RLD is not expected to provide accurate results, and biexponential fitting is required.

Numerous investigations have focused on efficient acquisition and fitting processes for both single^{20,25,26} and multiexponential^{21,27} decay applications. However, when a sample consists of multiple populations, such as in FRET, it can be particularly difficult to resolve parameter estimates for each population. Dense temporal sampling is therefore required to accurately estimate the multiexponential model parameters. Acquiring dense temporal and spatial information comes at the cost of increased acquisition times and potential photobleaching. For instance, acquisition time in time-gated fluorescence imaging is linearly related to the number of images, or time gates acquired; high rates of sampling, therefore, directly increase the time necessary to image the sample.^{28,29} This drawback is especially relevant to high-throughput and *in vivo* tomographic platforms, where lengthy acquisition times can prevent their widespread adoption due to hour-long imaging sessions. Hence, there is a need to identify strategies that estimate parameters for biexponential fitting based on temporal data reduction. In this study, we investigate the estimation accuracy of the fractional amplitude coefficients and their respective lifetimes of a biexponential model when employing a limited set of temporal data points. It will be shown that the number of time gates can be decreased by almost an order of magnitude with only minimal loss of accuracy. The study is framed within a NIR FRET application where the short-lifetime component is on the same time scale as the IRF. *In silico* experiments are performed to establish a strategy of time-point selection that preserves the parameter accuracy and results are validated with *in vitro* and *in vivo* imaging experimental data.

2 Materials and Methods

2.1 Time-Domain Wide-Field Gated Imaging

Generally, there are two main experimental techniques employed to acquire time-domain fluorescence decay curves over the typical range of fluorophore lifetimes employed in bioimaging: time-correlated single-photon counting and time-gated detection. Time-gated techniques are preferred, especially when large field of views and fast acquisition times are desired. In this work, we used a wide-field time-gated imaging platform working in the NIR range³⁰ and employed an active illumination module.^{31–33} This system has been designed to quantitatively image FRET donor fractions *in vitro*, *ex vivo*, and *in vivo*.^{29,31,34} Briefly, the system uses a Maitai laser as a source and is coupled to a digital micromirror unit (DLP Discovery 4100 Kit and D2D module, Texas Instruments Inc., Dallas, Texas) to obtain a spatially controllable wide-field excitation [or active wide-field illumination (AWFI)]. The fluorescence signals are collected in transmittance geometry via an ultrafast-gated, intensified CCD (ICCD) camera (Picostar HR, LaVision GmbH, Goettingen, Germany) which has a 12-bit CCD and a resolution of 1376×1040 pixels. For all experiments herein, the gate width size was set to 300 ps, the step size between gates to 40 ps, and the camera integration time to 800 ms. These settings were kept constant for both high-throughput FRET imaging in well plates and *in vivo* FRET imaging described in Secs. 2.4 and 2.5, respectively.

To ensure the acquisition of optimal fluorescence decay curves in terms of signal-to-noise ratio, an active illumination strategy was employed for all experimental data employed herein. In this approach, the illumination spatial distribution is actively and iteratively optimized to yield time fluorescence decay curves with maximum photon counts near the saturation level of the ICCD (3600 counts). Overall, this method allows for enhanced accuracy in lifetime-based imaging at high acquisition speed over samples with large fluorescence intensity distributions. We previously demonstrated that AWFI is able to accurately estimate lifetimes from a multiwell plate sample with concentrations ranging over 2 orders of magnitude, resulting in estimation error in quenched donor fraction of less than 6% (compared with optimally acquired, one-by-one analysis) over 18 well samples.³³

2.2 Biexponential and Noise Model

In the case of a population of two fluorophores with distinct lifetimes, the fluorescence decay curves can be accurately modeled using a biexponential model convolved with the IRF of the system.^{35,36} In such cases, the model is expressed as

$$I(t) = \text{IRF}(t) \otimes \left(A_1 e^{-\frac{t}{\tau_1}} + A_2 e^{-\frac{t}{\tau_2}} \right), \quad (1)$$

where $I(t)$ is the fluorescence decay, $\text{IRF}(t)$ is the instrument response function, \otimes is the convolution operator, and A_1 and A_2 are the fractional proportions of the lifetimes τ_1 and τ_2 , with $A_1 + A_2 = 1$. To estimate the main parameters of interest based on experimental data, this model is iteratively fit to the data using the LSQR method. The goodness-of-fit parameter, χ^2 , was used as a comparison and is defined as

$$\chi^2 = \sum_{k=1}^n \frac{[I(t_k) - I_C(t_k)]^2}{I_C(t_k)}, \quad (2)$$

where $I(t_k)$ is the fluorescence measurement at t_k , $I_C(t_k)$ is the fit value at the same time point, and n is the number of time points. Theoretically, four model parameters should be estimated when using the model of Eq. (1). However, this number of parameters can be reduced to A_1 and τ_1 for NIR FRET imaging. Owing to the relation $A_1 + A_2 = 1$, only one fractional amplitude needs to be estimated. Moreover, as the donor lifetime under no FRET condition is known *a priori*, either from the manufacturer data sheet or from the calibration experiments, it can be set as a constant in our model. Hence, herein, two parameters were fitted: A_1 and τ_1 .

This model was used to fit experimental data as well as to generate synthetic data to investigate the impact of the number and location of time gates on the estimation of the above-mentioned fitted parameters over a large range of functional values. To derive synthetic fluorescence measurements closely mimicking experimental data, the model in Eq. (1) was augmented via additive noise. Background noise, dark noise, and photon (shot) noise are generally the primary sources of noise in time-domain measurements.³⁷ Background noise can be limited by reducing the amount of ambient light incident on the system. All background noises are unlikely to be eliminated, and it must be measured and accounted for during the fitting process (usually via subtraction). Dark noise is kept to a minimum via active cooling of the ICCD. Shot noise follows a Poisson distribution and is due to the nonconstant absorption and emission of photons in response to a mean excitation signal. Though time-gated systems are not strictly shot noise limited, McGinty et al.⁶ have shown that the shot noise-like behavior is present when using common gain voltages. In practice, when modeling these systems, Poisson noise is usually the only added noise.^{38–40} Hence, an absolute Poisson noise was used as a good model for experimental noise in this study. As our experimental implementation benefits from active illumination, it yields homogeneous fluorescence time decay curves with maximum photon counts ~ 3600 ; all simulated data were normalized to this absolute count number. The Poisson noise was calculated at each gate and added to the pure fluorescence decay after convolution with the IRF to yield the synthetic data. Note that for the sake of comparison, RLD was also applied in certain cases with the formulation defined by Elangovan et al.⁴¹

2.3 In Silico Experimental Design

When acquiring *in vitro* and *in vivo* time-gated FLIM-FRETs, a few temporal parameters need to be specified *a priori*. First, the gate size and the step between gates need to be defined. Conventional gated systems based on gated ICCDs allow for a gate size between 200 and 1000 ps. Two-hundred-picosecond time gates are generally unstable, whereas large time gates, even if they lead to significantly faster acquisitions,⁴² oversmooth the fluorescence decays, leading to loss of accuracy in fitting.⁴³ Herein, as described in Sec. 2.1, the gate size was set to 300 ps and the step size between gates to 40 ps in all simulations to replicate optimal experimental conditions for FRET imaging. To avoid the confusion between gate numbers and their temporal locations, only gate numbers will be referenced in the remainder of this work. Because the step size is consistent, the temporal position of any time gate can be found by multiplying the

gate number by 40 ps (e.g., gate 10 is temporally located at approximately 400 ps after the peak of the decay). A total of 115 gates with equal step spacing were simulated to generate full fluorescence decay curves over a 4.6-ns temporal window. Second, when considering sparse temporal datasets, two parameters need to be defined: number of gates acquired and location of the gates. Herein, a brute-force approach based on large random trials is performed to investigate the impact of these two parameters on the estimation of FRET quantities.

First, a simulation is used to assess the information content of each individual time gate as quantified by the χ^2 value. To limit this investigation to a workable range of parameters, synthetic decay curves were created with model parameters set to $A_1 = 0.3$, $A_2 = 0.7$, $\tau_1 = 300$ ps, and $\tau_2 = 1200$ ps. These fractional amplitudes are frequently encountered in FRET applications, whereas the two lifetimes correspond to the lifetimes of the two states of the donor in the NIR FRET pair Alexa Fluor 700–Alexa Fluor 750 (see Sec. 2.4). Decay curves were generated using these model parameters convolved with an experimental IRF and with additive Poisson noise. After convolution, approximately 90 of the original 115 time gates fall within the decay portion of the curve and may be employed for fitting. For each simulated decay curve, four time gates in the decaying portion of the curve were randomly selected to constitute an initial dataset. This dataset was used to fit the curve and to retrieve the two FRET parameters identified above. As a merit function, the χ^2 value was saved and used as the starting reference. Then, the dataset was augmented by one time gate (five time gates total) and a new fitting procedure was carried out. The fitting procedure was carried out for all possible gates besides the initial four. The χ^2 values for all these fits were saved for postprocessing. The fifth gate among all remaining 86 gates that yielded the lowest χ^2 value was selected to create a new reference five time-gate dataset. Expectedly, this additional time gate provided the most significant additional information content to the original four time gates. This process was repeated to assess which remaining gates most increased the fitting quality when augmenting the dataset from five gates to a total of 14 gates, one gate at a time. Then, as the original four time-gate datasets were randomly selected, they were removed to yield the optimal 10 time-gate dataset. The process was not carried over 10 additional time gates to keep the simulation tractable. This complete process was repeated 1000 times to minimize the bias from the random selection of the four initial gates and additive random noise. A flowchart is provided in Fig. 1(a). Typical examples of initial datasets and additional temporal points are provided in Figs. 1(b)–1(e).

Second, we investigated the effect the number of time gates used had on the accuracy of model parameter estimation. Another randomized trial was performed using the same procedure to generate the synthetic data. Based on the findings in the previous study (see Sec. 3), the selected time gates were evenly spaced on the decaying part of the curve after IRF convolution. Overall, datasets consisting of 90 (all), 45, 23, 10, six, or four time gates were investigated herein. Using the same model parameters as the previous experiment ($A_1 = 0.3$, $A_2 = 0.7$, $\tau_1 = 300$ ps, and $\tau_2 = 1200$ ps), parameter estimation accuracy was evaluated for each set of time gates over 1000 runs, to avoid the bias caused by the noise generation process. Then, the model parameter range was expanded to encompass the entire range of likely parameter values under

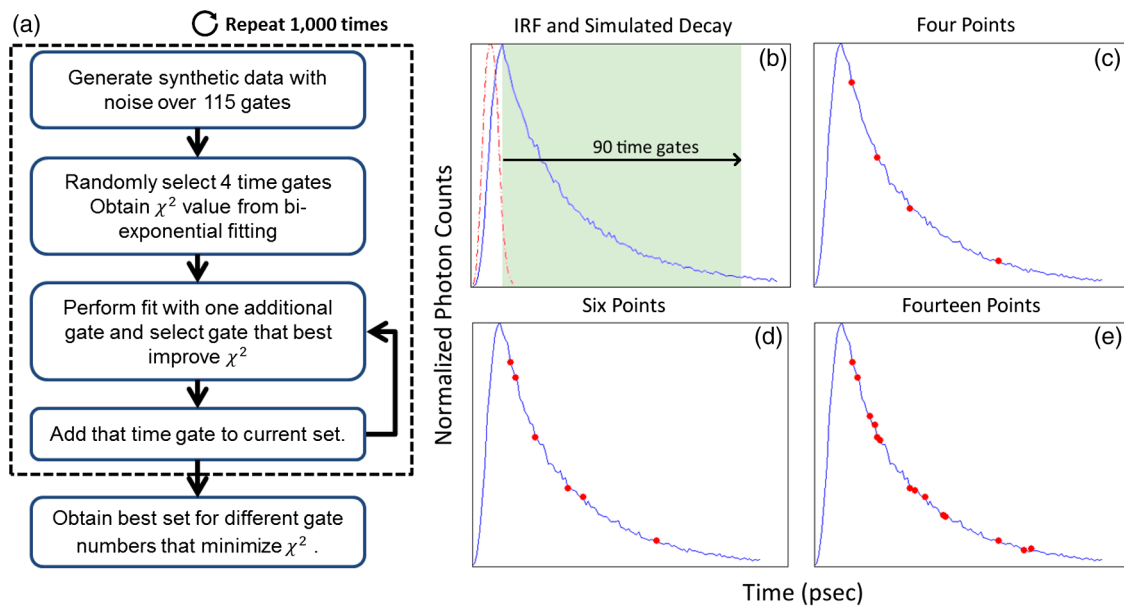


Fig. 1 (a) Workflow of the *in silico* study. First, noisy synthetic data are generated over a 4.6-ns temporal window and χ^2 is estimated using four random time gates as the measurement dataset. Then, best additional gates are estimated iteratively until the dataset is comprised of 14 gates. The overall process is reproduced 1000 times. (b) A representative experimental IRF and synthetic fluorescence decay curve are shown; the solid area corresponds to the temporal range of 90 time gates that may be used for fitting. (c–e) A representative decay at several iterations in the gate selection process.

experimental conditions. A_1 and A_2 were varied from 0.1 to 0.9 by increments of 0.1 (keeping the relationship $A_1 + A_2 = 1$), while τ_1 was varied from 250 to 450 ps in increments of 25 ps. The lifetime of the unquenched donor (τ_2) was kept at 1200 ps throughout the simulation. To keep the computational burden manageable, 100 decay curves per set of time gates and model parameters were generated as synthetic data. The fitting procedure was applied to each of these 48,600 synthetic curves.

2.4 Cell Assay Data

An *in vitro* FRET assay experiment was used to validate the outcome of the *in silico* study. More precisely, we employed a NIR FRET transferrin (Tfn) assay in 96-well plate settings. Tfn has been used as a carrier for anticancer drugs or other therapeutic agents^{44–46} to enhance the internalization specificity into neoplastic tissues. The Tfn receptor (TfnR) is homodimeric, i.e., two molecules of Tfn bind within 2 to 10 nm, which allows the use of FRET-based imaging techniques.⁴⁷ By detecting FRET between a FRET pair labeled with Tfn molecules, we are able to quantitatively determine whether Tfn is bound to TfnR at the plasma membrane and along the endocytic pathway (FRET positive signals).^{48–52} As we are focusing on macroscopic *in vitro* or *in vivo* assays, the data collected by our system at each pixel are a mixture of quenched (FRET positive signals) and unquenched (FRET negative signals) fluorescence signals of the donor. Hence, they exhibit a typical biexponential decay as modeled by Eq. (1). If the short-lifetime component is represented by τ_1 (FRET positive signals), then the parameter of particular interest is A_1 , as it represents the quenched fraction of the FRET donor, or in our application, the internalized amount of Tfn.^{29,31,33,34}

Here, human Tfn molecules labeled with a NIR FRET pair (Alexa Fluor 700–Alexa Fluor 750) were added to Madin–Darby canine kidney (MDCK) cells and T47D cells (human

ductal breast epithelial tumor cell line), both lines expressing human TfnR.^{34,48,49} This specific FRET pair was chosen due to the significant spectral overlap and Förster distance (≈ 7.76 nm). Furthermore, it was found to perform the best for this application compared with five other FRET pairs.²⁴ Six different acceptor to donor (AD) ratios (0:1, 1:3, 1:2, 1:1, 2:1, and 3:1) were employed to establish FRET parameter estimation accuracy versus temporal data sparsity. The configuration of the multiwell plate and fluorescence intensity (at peak maximum) is provided in Fig. 2(a). By design, a linear

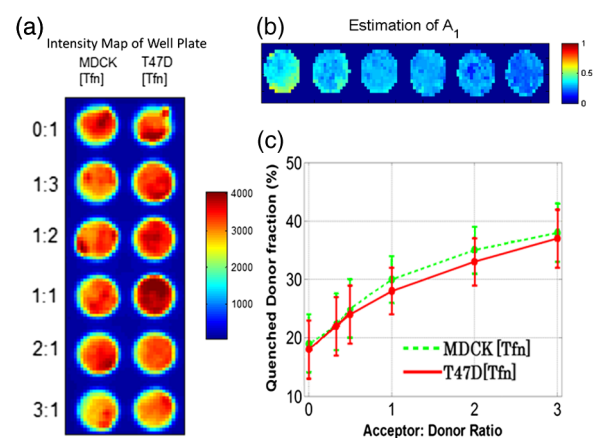


Fig. 2 (a) Example results of photon counts at the maximum of the decay curve with different cell lines and AD ratios over the 12 wells. The counts are close to the maximum photon counts that can be acquired by the gated ICCD thanks to AWFI. (b) Example of model parameter estimation over row 1 (MDCK) of the sample. Here only A_1 is depicted, as it is the parameter of interest for the application. (c) Quenched donor fraction (A_1) estimation over the whole sample. Mean values for each well with standard deviation are reported when estimated with the full temporal dataset.

relationship between quenched donor fraction and AD is expected for these two cell types over the range of AD ratios used. The estimation using all available time points serves as our benchmark when comparing results obtained with sparse temporal datasets [cf. Figs. 2(b) and 2(c)].

2.5 In Vivo Data

An athymic nude female mouse (6- to 12-week-old—BALBBNU-F Taconic, Rensselaer, New York) was used for *in vivo* validation. The mouse was injected with Tfn-labeled AF750 (AF750-Tfn) and Tfn-labeled AF700 (AF700-Tfn) in RPMI 1640 media at molar ratios of 2:1 (keeping the donor amounts constant at 40 $\mu\text{g}/\text{ml}$ of Tfn) via the tail vein using a sterile 1-mL syringe and 27.5-gauge needle.³⁴ The mouse was imaged 2 h postinjection using the system described by Venugopal et al.²⁹ The technique uses transmitted light via fluorescence molecular tomography, adaptive wide-field tomography, and Monte Carlo-based propagation models to perform three-dimensional (3-D) reconstruction of FRET activity. The live animal imaging was performed under vapor anesthesia (EZ-SA800 System, E-Z Anesthesia, Palmer, Pennsylvania) using isoflurane and monitored using a physiological monitoring system (MouseOx Plus, STARR Life Sciences Corp., Oakmont, Pennsylvania). Body temperature was maintained by an air warmer (Bair Hugger 50500, 3M Corporation, St. Paul, Minnesota) during the entire imaging session. All animal protocols were conducted with approval by the Institutional Animal Care and Use Committee at both Albany Medical College and Rensselaer Polytechnic Institute.

3 Results and Discussion

3.1 In Silico

First, the 10 best time gates defined as the ones leading to the best χ^2 value when fitting the synthetic data were identified. Due to the large number of datasets investigated, we report only the number of occurrences in which a specific time gate has been identified in the optimal 10-time-gate dataset. This information is reported as a histogram in Fig. 3(a). Overall, the data are skewed toward the first time gate (peak maximum). Selection frequency decreases as moving to the right of the histogram. This result suggests that the early time components are especially important for fitting accuracy in biexponential fitting. This agrees with intuition, as the beginning of the biexponential decay has the greatest slope rate of change and thus

would benefit more from frequent sampling than the later portions. To test this theory, uneven sampling sets of 10 time gates were evaluated against even sampling sets in addition to the complete set of time gates. Figure 3(b) shows a representative example of fitting parameter results for even versus uneven temporal samplings. The uneven sampling set consisted of the following time gates: 1, 2, 3, 4, 5, 10, 30, 50, 70, and 90. In all three cases, fitting accuracy of the model parameters was within 6% of the expected values and the differences between them were not significant. Note that many uneven sampling sets were evaluated with similar outcomes, indicating that an even temporal sampling may work similarly well compared with a set of unevenly spaced time gates chosen based upon *a priori* knowledge of the system. This is a significant result in terms of experimental implementation. Without *a priori* knowledge of the fluorophores' exact fractional distribution and location in tissue, it is difficult to know the position of the main temporal features of the fluorescence data (maximum count position, for instance). Hence, it is difficult to implement the nonlinear temporal sampling as no temporal references are known. However, acquisition based on even temporal distribution of time gates can be easily and efficiently implemented without prior knowledge. Based on these results, evenly spaced time gates are employed exclusively in the remainder of this work.

Second, the effect of the number of time gates on fitting accuracy was investigated using the same model parameters and with 1000 runs. The errors associated with the two estimated model parameters are provided in Fig. 4. For comparison, we provide both estimation errors for LSQR and RLD methods. As expected, at the nominal parameter values of $A_1 = 0.3$ and $\tau_1 = 300$ ps, the error increases as fewer time gates are considered, error being defined as the difference between simulated and mean of the estimations. The error between the estimate and model for A_1 was within 6% and for τ_1 was within 4% (11 ps) in the case where all time gates are used. The error in the estimation of parameters when using full datasets can be attributed to the ill-posedness of the biexponential fits and Poisson noise. Similar levels of uncertainty are maintained using up to 10 gates for fitting. When reducing the number of time gates further, the errors increase up to 22% when using only four gates. A similar trend can be observed when focusing on the standard deviation for the error estimation, based on the 1000 trials. Hence, these results suggest that fitting with 10 equally spaced gates yields similar results as using full temporal datasets (90 gates). Note that RLD is generally unstable with a short lifetime of size similar to that of the IRF. The

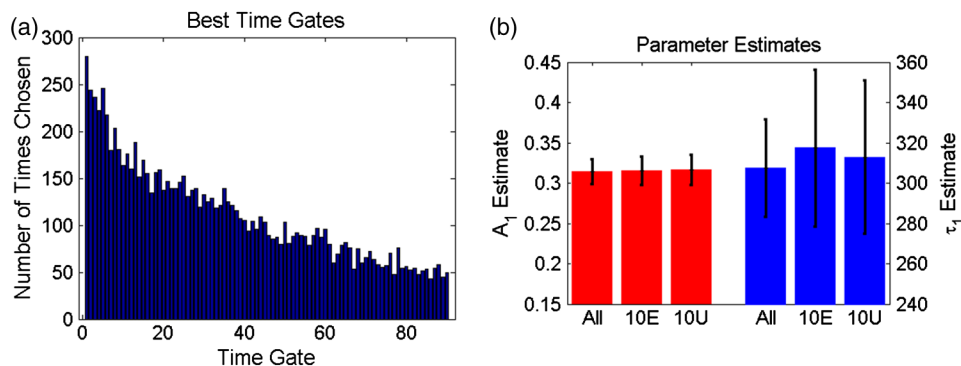


Fig. 3 (a) Histogram of the number of occurrences that a specific time gate position (#) is present in the 1000 optimal temporal datasets. (b) Parameter estimates over 1000 runs using 10 evenly spaced (10E) time gates and 10 unevenly spaced (10U) time gates compared with using all available time gates.

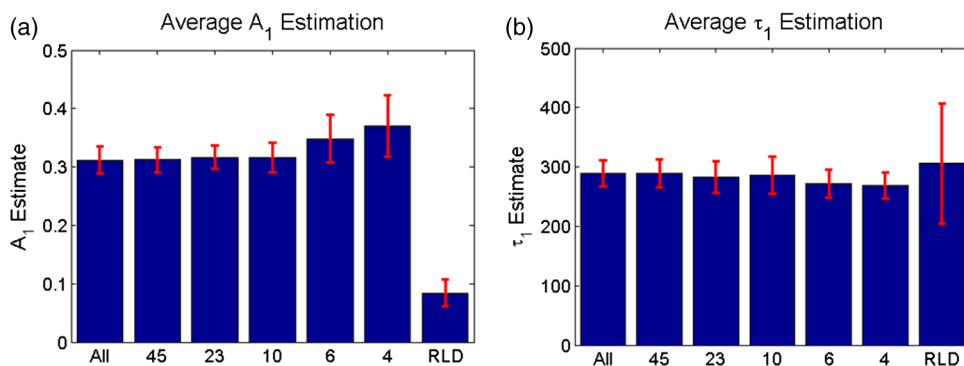


Fig. 4 Average and standard error associated with parameter estimation when using sparse temporal datasets and RLD for model parameters (a) A_1 and (b) τ_1 . The expected values are 0.3 and 300, respectively.

average error for A_1 was about 90%, and the average error for τ_1 was 2% over 1000 runs, but with a standard deviation of more than 100 ps.

To assess if these findings were dependent on the model parameters, these error functions were estimated over a full functional range of values that can be encountered in biexponential applications. Results are given in Fig. 5. The trend is similar when the experiment is expanded across the entire parameter space. Average error in A_1 across all parameter combinations using all time gates was within 5% and increased to 19% (with local peak errors approaching 60%) using four time gates. Again, a large increase in the average error across all combinations occurs when the number of time gates is reduced from 10 (6%) to 6 (14%). For small fractional amplitudes ($A_1 \in [0.1$ to $0.2]$), the error in A_1 using six and four time gates significantly increases for all values of τ_1 , ranging from 40% to 60%. Overall, these simulations establish that using 10 time gates results in similar estimation accuracy as using full temporal data for the parameter range of $\tau_1 \in [250$ to $450]$ ps and $A_1 \in [0.1$ to $0.9]$. The average error in estimating A_1 across the entire parameter space was increased by only 1% when sampling down the temporal data from 90 gates to 10 gates. A reduction in time-gate acquisition of this magnitude would result in almost

a 10-fold decrease in acquisition time required, while yielding the same biological insights based on model parameters fitted.

3.2 Validation In Vitro and In Vivo

In order to validate the results obtained from *in silico* simulations, the findings are applied to cell-based assay and *in vivo* experiments. Experimental results were originally acquired using 120 time gates, approximately 90 of which fall in the asymptotic part of the measurements. Parameter estimation is performed using the entire set of available time gates in addition to using reduced subsets of time gates. Of particular interest in each of these experimental procedures is A_1 , the quenched donor fraction, which represents the fraction of Tfn bound donor that underwent cellular internalization. Data were acquired using wide-field excitation and acquisition, as described in Sec. 2.4. A comparison of estimation errors in A_1 for a subset of the data is made in Table 1 and Fig. 6. Table 1 shows a subset of the results for both cell lines compared with previous simulation results. The data agree well with the results from simulations with a similar trend occurring in all three datasets. In both cell lines, the error is approximately the same when using 90, 45, 23, or 10 time gates in addition

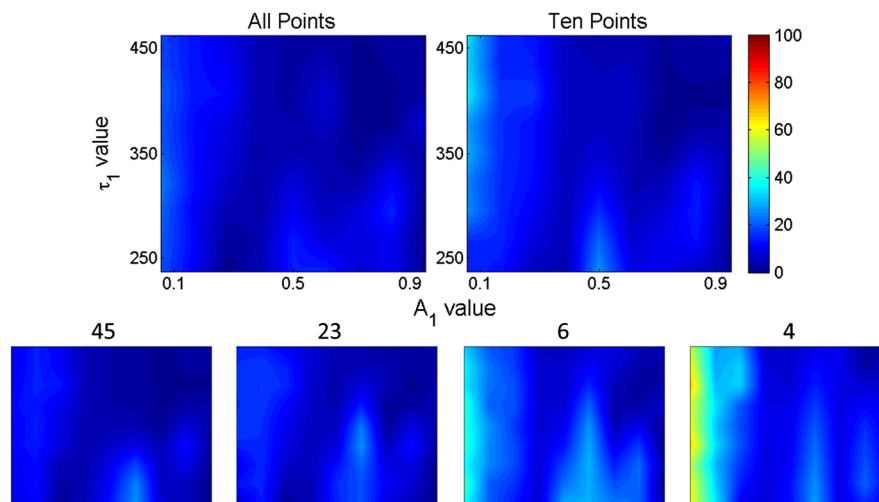


Fig. 5 Percent error in A_1 estimation when using different numbers of gates (90, 45, 23, 10, six, and four) for $\tau_1 \in [250$ to $450]$ ps and $A_1 \in [0.1$ to $0.9]$.

Table 1 A subset of the A_1 estimates (error % in parenthesis) using *in vitro* data and different sets of time gates compared with simulation results. *In vitro* data are from wells with an AD ratio of 0:1.

Number of time gates	All	45	23	10	6	4
Simulation	(6)	(6)	(7)	(7)	(14)	(18)
T47D	18.9 ± 5 (5)	18.8 ± 5 (4)	18.9 ± 5 (5)	19.0 ± 5 (6)	15.8 ± 5 (12)	14.2 ± 6 (21)
MDCK	18.8 ± 7 (4)	18.8 ± 7 (4)	18.7 ± 7 (4)	19.0 ± 7 (6)	16.1 ± 7 (10)	13.9 ± 8 (23)

to having similar standard deviations. Like the *in silico* experiments, there is also a large increase in error between using 10 and 6 time gates. Figure 6 shows the A_1 estimates from the T47D cell line across all AD ratios using several subsets of gates. Results using all or 10 time gates have similar mean estimates and standard deviations, whereas the results using four time gates tend to have larger standard deviations and different means. Note, however, that in all cases, the linear trend with increasing AD ratio is present and is similar to the result in Fig. 2(c).

In vivo data were collected as described in Sec. 2.5. The data were fitted using the complete (90) set of time gates as well as

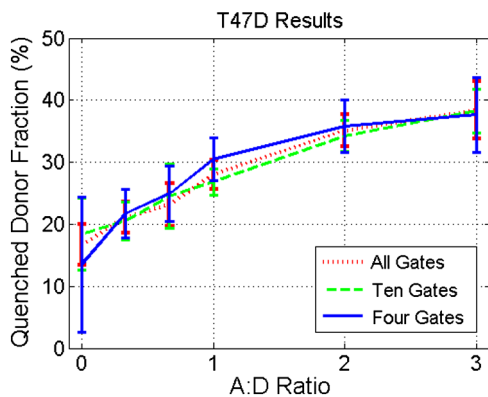


Fig. 6 Estimation of A_1 using *in vitro* experimental data (T47D cell line) and all, 10, or four time gates. The linear relationship in AD ratio is retained in all cases; however, using 10 time gates more accurately tracks the linear relationship.

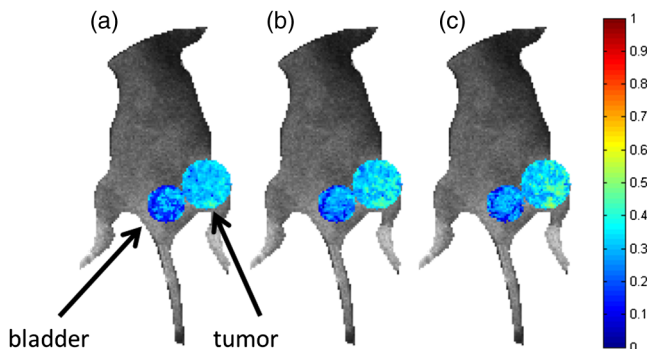


Fig. 7 Comparison of *in vivo* estimations of A_1 in the bladder and the tumor (larger circle) of a mouse using (a) all time gates, (b) 10 time gates, and (c) four time gates. The estimations have been overlaid on a bright field image to provide the context. Results are largely similar with the bladder having a lower average A_1 estimate than the tumor, as expected.

the reduced sets of 10 and four time gates. The quenched donor fraction (A_1) was estimated in the tumor of the mouse in addition to the bladder as shown in Fig. 7. The mean A_1 estimates in the tumor are greater than in the bladder using each set of time gates (cf. Table 2). In each case, using 10 time gates results in similar mean estimates and little or no difference in standard deviation compared with using 90 time gates. The means vary by an average of approximately 4%, but because there is no ground truth information available, the total difference in error is not measurable. Using four time gates results in a higher average difference in mean of approximately 7% in addition to a larger standard deviation compared with using 90 time gates. Note that these results are consistent with the expected physiological results. The tumor model employed herein overexpresses TfnR, whereas minimal FRET Tfn is expected in the bladder. Hence, it is expected that the tumor would exhibit a larger mean A_1 as higher values of A_1 represent a larger portion of Tfn on the endocytic pathway.

3.3 Discussion

Overall, these results suggest that by reducing the total number of time gates acquired from 90 to 10, FLIM-FRET acquisition time can be reduced by approximately an order of magnitude without greatly sacrificing the estimation accuracy. This is a significant result, especially for *in vitro* and *in vivo* platforms where FLIM-FRET techniques have yet to be widely adopted because of lengthy imaging times. Imaging platforms designed for drug discovery applications have recently been described by Talbot et al.⁵³ and Alibhai et al.⁵⁴ to take 30 and 46 min., respectively, to acquire a 96-well plate. By applying the methods described herein, a 96-well plate could be imaged in less than 1 min. These short acquisition times are particularly attractive for high-throughput FRET assays. Not only will such a platform be able to greatly increase the number of wells imaged in one session, but it will also permit increased multiplexing to significantly increase the number of processes studied. This will

Table 2 A comparison of *in vivo* A_1 estimates using different sets of time gates. Using 10 time gates to fit the data results in similar estimates with similar standard deviations to the case of using all time gates. Using four time gates results in larger standard deviations and less accurate estimations, especially in the tumor.

Number of time gates	All	10	4
Bladder	0.22 ± 0.07	0.23 ± 0.07	0.23 ± 0.08
Tumor	0.32 ± 0.04	0.33 ± 0.04	0.35 ± 0.07

prove critical in enabling the design and optimization of new therapies using *in vitro* FLIM-FRET platforms.

Moreover, we have recently demonstrated that our novel wide-field imaging FLIM-FRET approach offers the possibility to employ well-characterized quantitative metrics used in FRET microscopy, but with the additional benefit of a seamless technological platform to perform *in vivo* quantitative assays. Based on wide-field patterned time-resolved illumination and gated detection,⁵⁵ we demonstrated that it was possible to retrieve in 3-D the quantitative biodistribution of the quenched donor fraction within 5% of *in vitro* data. However, as multiple projections are required to resolve the depth information based on an optical inverse problem,^{56–58} the imaging protocols typically take around 45 min for whole-body imaging. In comparison, current time-resolved tomography platforms typically are able to image only cross-sections (two dimensional) of the animal and require imaging acquisition times of between 30 and 45 min.^{59,60} Similar to *in vitro* data, temporal data reduction can lead to reduced acquisition times. Based on the findings of this work, we expect to be able to perform the whole-body 3-D FLIM-FRET in live animals in less than 5 min. Such fast acquisition speed will enable investigation of locally resolved fast pharmacokinetics studies *in vivo*, imaging multiple FRET pairs sequentially in reasonable time frames, and an increase in overall imaging throughput. These developments will be critical to establish FLIM-FRET as a reliable and attractive quantitative assay to the biomedical community for *in vivo* applications.

4 Conclusion

The *in silico* experiments performed herein suggest that acquiring an even distribution of time gates throughout the decay curve results in maximal information content of the curve. Additionally, it has been shown that using 10 time gates results in essentially no increase in average estimation error of A_1 compared with using 90 time gates. Results were then validated in both *in vitro* and *in vivo* settings by performing the parameter estimation using a reduced set of acquired time gates. By reducing the number of time gates acquired to 10, acquisition times can be reduced by almost 10-fold. This reduction in acquisition time for time-gated FLIM-FRET will open the door for the implementation of FLIM-FRET methods in high-content analysis and high-throughput screening. Usage of equally spaced time gates ensures that this is immediately implementable on time-gated systems for *in vitro*, *ex vivo*, and *in vivo* applications.

Acknowledgments

The authors thank K. Abe, S. Rajoria, and M. Barroso (Albany Medical College, The Center for Cardiovascular Sciences, Albany, New York 12208) for help with the *in vitro* and *in vivo* assays. This work was partly funded by the National Institutes of Health Grant R21 CA161782 and R21 EB013421 and National Science Foundation CAREER AWARD CBET-1149407.

References

- H. Wallrabe and A. Periasamy, "Imaging protein molecules using FRET and FLIM microscopy," *Curr. Opin. Biotechnol.* **16**(1), 19–27 (2005).
- M. Y. Berezin and S. Achilefu, "Fluorescence lifetime measurements and biological imaging," *Chem. Rev.* **110**(5), 2641–2684 (2010).
- M. Hassan et al., "Fluorescence lifetime imaging system for *in vivo* studies," *Mol. Imaging* **6**(4), 229–236 (2007).

- P. I. H. Bastiaens and A. Squire, "Fluorescence lifetime imaging microscopy: spatial resolution of biochemical processes in the cell," *Trends Cell Biol.* **9**(2), 48–52 (1999).
- A. Pliss et al., "Fluorescence lifetime of fluorescent proteins as an intracellular environment probe sensing the cell cycle progression," *ACS Chem. Biol.* **7**(8), 1385–1392 (2012).
- J. McGinty et al., "In vivo fluorescence lifetime tomography of a FRET probe expressed in mouse," *Biomed. Opt. Express* **2**(7), 1907–1917 (2011).
- V. Gaiand et al., "Towards *in vivo* imaging of intramolecular fluorescence resonance energy transfer parameters," *J. Opt. Soc. Am. A* **26**(8), 1805–1813 (2009).
- S. S. Vogel, C. Thaler, and S. V. Koushik, "Fanciful FRET," *Sci. STKE* **2006**(331), re2 (2006).
- J. R. Lakowicz et al., "Fluorescence lifetime imaging of intracellular calcium in COS cells using Quin-2," *Cell Calcium* **15**(1), 7–27 (1994).
- J. R. Lakowicz, *Principles of Fluorescence Spectroscopy*, 3rd ed., Springer, New York (2006).
- K. M. Hanson et al., "Two-photon fluorescence lifetime imaging of the skin stratum corneum pH gradient," *Biophys. J.* **83**(3), 1682–1690 (2002).
- E. M. Merzlyak et al., "Bright monomeric red fluorescent protein with an extended fluorescence lifetime," *Nat. Methods* **4**(7), 555–557 (2007).
- R. B. Sekar and A. Periasamy, "Fluorescence resonance energy transfer (FRET) microscopy imaging of live cell protein localizations," *J. Cell Biol.* **160**(5), 629–633 (2003).
- A. Miyawaki, "Development of probes for cellular functions using fluorescent proteins and fluorescence resonance energy transfer," *Annu. Rev. Biochem.* **80**(1), 357–373 (2011).
- S. Kumar et al., "FLIM FRET technology for drug discovery: automated multiwell-plate high-content analysis, multiplexed readouts and application *in situ*," *Chemphyschem* **12**(3), 609–626 (2011).
- S. Rajoria et al., "FLIM-FRET for cancer application," *Curr. Mol. Imaging* (in press).
- W. Becker, "Fluorescence lifetime imaging—techniques and applications," *J. Microsc.* **247**(2), 119–136 (2012).
- E. Gratton et al., "Fluorescence lifetime imaging for the two-photon microscope: time-domain and frequency-domain methods," *J. Biomed. Opt.* **8**(3), 381–390 (2003).
- S. B. Keller et al., "Calibration approach for fluorescence lifetime determination for applications using time-gated detection and finite pulse width excitation," *Anal. Chem.* **80**(20), 7876–7881 (2008).
- R. M. Ballew and J. N. Demas, "An error analysis of the rapid lifetime determination method for the evaluation of single exponential decays," *Anal. Chem.* **61**(1), 30–33 (1989).
- K. K. Sharman et al., "Error analysis of the rapid lifetime determination method for double-exponential decays and new windowing schemes," *Anal. Chem.* **71**(5), 947–952 (1999).
- G. Zheng et al., "Contrast-enhanced near-infrared (NIR) optical imaging for subsurface cancer detection," *J. Porphyrins Phthalocyanines* **08**(09), 1106–1117 (2004).
- Y. Chen et al., "Near-infrared phase cancellation instrument for fast and accurate localization of fluorescent heterogeneity," *Rev. Sci. Instrum.* **74**(7), 3466–3473 (2003).
- N. Sinsuebphon et al., "Comparison of NIR FRET pairs for quantitative transferrin-based assay," *Proc. SPIE* **8937**, 89370X (2014).
- C.-W. Chang and M.-A. Mycek, "Improving precision in time-gated FLIM for low-light live-cell imaging," *Proc. SPIE* **7370**, 737009 (2009).
- P. D. Waters and D. H. Burns, "Optimized gated detection for lifetime measurement over a wide range of single exponential decays," *Appl. Spectrosc.* **47**(1), 111–115 (1993).
- C. J. de Grauw and H. C. Gerritsen, "Multiple time-gate module for fluorescence lifetime imaging," *Appl. Spectrosc.* **55**(6), 670–678 (2001).
- S. Padilla-Parra et al., "Quantitative FRET analysis by fast acquisition time domain FLIM at high spatial resolution in living cells," *Biophys. J.* **95**(6), 2976–2988 (2008).
- V. Venugopal et al., "Quantitative tomographic imaging of intermolecular FRET in small animals," *Biomed. Opt. Express* **3**(12), 3161–3175 (2012).

30. V. Venugopal, J. Chen, and X. Intes, "Development of an optical imaging platform for functional imaging of small animals using wide-field excitation," *Biomed. Opt. Express* **1**(1), 143–156 (2010).
31. L. Zhao et al., "Spatial light modulator based active wide-field illumination for ex vivo and in vivo quantitative NIR FRET imaging," *Biomed. Opt. Express* **5**(3), 944–960 (2014).
32. V. Venugopal and X. Intes, "Adaptive wide-field optical tomography," *J. Biomed. Opt.* **18**(3), 036006 (2013).
33. L. Zhao et al., "Active wide-field illumination for high-throughput fluorescence lifetime imaging," *Opt. Lett.* **38**(19), 3976–3979 (2013).
34. K. Abe et al., "Non-invasive in vivo imaging of near infrared-labeled transferrin in breast cancer cells and tumors using fluorescence lifetime FRET," *PLoS ONE* **8**(11), e80269 (2013).
35. M. Peter and S. M. Ameer-Beg, "Imaging molecular interactions by multiphoton FLIM," *Biol. Cell* **96**(3), 231–236 (2004).
36. P. R. Barber et al., "Global and pixel kinetic data analysis for FRET detection by multi-photon time-domain FLIM," *Proc. SPIE* **5700**, 171–181 (2005).
37. T. J. Brukilacchio, "A diffuse optical tomography system combined with x-ray mammography for improved breast cancer detection," PhD Thesis, Tufts University (2003).
38. F. Fereidouni, K. Reitsma, and H. C. Gerritsen, "High speed multispectral fluorescence lifetime imaging," *Opt. Express* **21**(10), 11769–11782 (2013).
39. D. S. Elson et al., "Real-time time-domain fluorescence lifetime imaging including single-shot acquisition with a segmented optical image intensifier," *New J. Phys.* **6**(1), 180 (2004).
40. A. Leray et al., "Spatio-temporal quantification of FRET in living cells by fast time-domain FLIM: a comparative study of non-fitting methods," *PLoS ONE* **8**(7), e69335 (2013).
41. M. Elangovan, R. N. Day, and A. Periasamy, "Nanosecond fluorescence resonance energy transfer-fluorescence lifetime imaging microscopy to localize the protein interactions in a single living cell," *J. Microsc.* **205**(1), 3–14 (2002).
42. V. Venugopal, "A small animal time-resolved optical tomography platform using wide-field excitation," PhD Thesis, Rensselaer Polytechnic Institute (2011).
43. F. Fereidouni et al., "A modified phasor approach for analyzing time-gated fluorescence lifetime images: time-gated phasor approach," *J. Microsc.* **244**(3), 248–258 (2011).
44. C. H. J. Choi et al., "Mechanism of active targeting in solid tumors with transferrin-containing gold nanoparticles," *Proc. Natl. Acad. Sci. U. S. A.* **107**(3), 1235–1240 (2010).
45. H. Zhuo et al., "Tumor imaging and interferon- γ -inducible protein-10 gene transfer using a highly efficient transferrin-conjugated liposome system in mice," *Clin. Cancer Res.* **19**(15), 4206–4217 (2013).
46. Z. M. Qian et al., "Targeted drug delivery via the transferrin receptor-mediated endocytosis pathway," *Pharmacol. Rev.* **54**(4), 561–587 (2002).
47. Y. Sun et al., "FRET microscopy in 2010: the legacy of Theodor Förster on the 100th anniversary of his birth," *Chemphyschem* **12**(3), 462–474 (2011).
48. R. Talati et al., "Automated selection of regions of interest for intensity-based FRET analysis of transferrin endocytic trafficking in normal vs. cancer cells," *Methods* **66**(2), 139–152 (2014).
49. A. Periasamy et al., "Quantitation of protein-protein interactions: confocal FRET microscopy," *Methods Cell Biol.* **89**, 569–598 (2008).
50. H. Wallrabe et al., "Receptor complexes cotransported via polarized endocytic pathways form clusters with distinct organizations," *Mol. Biol. Cell* **18**(6), 2226–2243 (2007).
51. H. Wallrabe et al., "Issues in confocal microscopy for quantitative FRET analysis," *Microsc. Res. Tech.* **69**(3), 196–206 (2006).
52. H. Wallrabe et al., "Confocal FRET and FLIM microscopy to characterize the distribution of transferrin receptors in membranes," *Proc. SPIE*, **6089**, 608905 (2006).
53. C. B. Talbot et al., "High speed unsupervised fluorescence lifetime imaging confocal multiwell plate reader for high content analysis," *J. Biophotonics* **1**(6), 514–521 (2008).
54. D. Alibhai et al., "Automated fluorescence lifetime imaging plate reader and its application to Förster resonant energy transfer readout of Gag protein aggregation," *J. Biophotonics* **6**(5), 398–408 (2013).
55. J. Chen et al., "Time-resolved diffuse optical tomography with patterned-light illumination and detection," *Opt. Lett.* **35**(13), 2121–2123 (2010).
56. J. Chen, Q. Fang, and X. Intes, "Mesh-based Monte Carlo method in time-domain widefield fluorescence molecular tomography," *J. Biomed. Opt.* **17**(10), 106009 (2012).
57. J. Chen and X. Intes, "Comparison of Monte Carlo methods for fluorescence molecular tomography—computational efficiency," *Med. Phys.* **38**(10), 5788–5798 (2011).
58. M. Pimpalkhare et al., "Ex vivo fluorescence molecular tomography of the spine," *Int. J. Biomed. Imaging* **2012**, e942326 (2012).
59. M. J. Niedre et al., "Early photon tomography allows fluorescence detection of lung carcinomas and disease progression in mice in vivo," *Proc. Natl. Acad. Sci. U. S. A.* **105**(49), 1–6 (2008).
60. K. M. Tichauer et al., "Imaging workflow and calibration for CT-guided time-domain fluorescence tomography," *Biomed. Opt. Express* **2**(11), 3021–3036 (2011).

Travis Omer received his BS degree in mechanical engineering from Brigham Young University in 2012. Currently, he is pursuing a PhD degree in biomedical engineering at Rensselaer Polytechnic Institute. His interests are in systems modeling, analysis, and optimization and specifically as they are applied to biomedical applications.

Lingling Zhao is a PhD student in the Department of Biomedical Engineering at Rensselaer Polytechnic Institute. She earned her MS degree in electrical engineering at the University at Buffalo in 2010. Her research interests are fluorescence lifetime imaging and diffuse functional and fluorescence molecular optical techniques for biomedical imaging in preclinical applications.

Xavier Intes is an associate professor in the Department of Biomedical Engineering at Rensselaer Polytechnic Institute. He obtained his PhD degree from Université de Bretagne Occidentale and postdoctoral training at the University of Pennsylvania. He acted as the chief scientist of Advanced Research Technologies Inc. from 2003 to 2006. His research interests are on the application of diffuse functional and molecular time-resolved optical techniques for biomedical imaging in preclinical and clinical settings.

Juergen Hahn received his PhD degree from the University of Texas, Austin. He joined Texas A&M University in 2003 and moved to the Rensselaer Polytechnic Institute as a professor in 2012. He is currently heading the Department of Biomedical Engineering in addition to holding an appointment in the Department of Chemical & Biological Engineering. His research interests include systems biology and process modeling and analysis with over 75 articles and book chapters in print.